

Article

Internal Solitary Waves in the Andaman Sea: New Insights from SAR Imagery

Jorge M. Magalhaes ^{1,2}  and José C. B. da Silva ^{1,2,*} 

¹ Department of Geosciences, Environment and Spatial Planning (DGAOT), Faculty of Sciences, University of Porto, 4169-007 Porto, Portugal; jmagalhaes@fc.ul.pt

² Interdisciplinary Centre of Marine and Environmental Research (CIIMAR), 4450-208 Matosinhos, Portugal

* Correspondence: jdasilva@fc.up.pt; Tel.: +351-220-402-476

Received: 30 April 2018; Accepted: 28 May 2018; Published: 1 June 2018



Abstract: The Andaman Sea in the Indian Ocean has been a classical study region for Internal Solitary Waves (ISWs) for several decades. Papers such as Osborne and Burch (1980) usually describe mode-1 packets of ISWs propagating eastwards, separated by distances of around 100 km. In this paper, we report on shorter period solitary-like waves that are consistent with a mode-2 vertical structure, which are observed along the Ten Degree Channel, and propagate side-by-side the usual large mode-1 solitary wave packets. The mode-2 waves are identified in TerraSAR-X images because of their distinct surface signatures, which are reversed when compared to those that are typical of mode-1 ISWs in the ocean. These newly observed regularly-spaced packets of ISW-like waves are characterized by average separations of roughly 30 km, which are far from the nominal mode-1 or even the mode-2 internal tidal wavelengths. On some occasions, five consecutive and regularly spaced mode-2 ISW-like wave envelopes were observed simultaneously in the same TerraSAR-X image. This fact points to a tidal generation mechanism somewhere in the west shallow ridges, south of the Nicobar Islands. Furthermore, it implies that unusually long-lived mode-2 waves can be found throughout the majority of the fortnightly tidal cycle. Ray tracing techniques are used to identify internal tidal beams as a possible explanation for the generation of the mode-2 solitary-like waves when the internal tidal beam interacts with the ocean pycnocline. Linear theory suggests that resonant coupling with long internal waves of higher-mode could explain the longevity of the mode-2 waves, which propagate for more than 100 km. Owing to their small-scale dimensions, the mode-2 waves may have been overlooked in previous remote sensing images. The enhanced radiometric resolution of the TerraSAR-X, alongside its wide coverage and detailed spatial resolutions, make it an ideal observational tool for the present study.

Keywords: SAR; internal waves; Andaman Sea

1. Introduction

Efficiently monitoring the ocean by means of satellite imagery is becoming an increasingly valuable tool, as its surveying ability on a global basis is far beyond that of traditional in situ measurements. Satellite remote sensing especially excels in acquiring and integrating multiple views of the ocean including in synergy with numerical modelling and in situ data, and hence it leverages our ability to document, understand, and predict a wide range of ocean phenomena. In particular, orbiting Synthetic Aperture Radars (SARs) have been acquiring high-resolution radar images in all-weather conditions for nearly four decades—since Seasat first flew in 1978. Their unique views of the ocean surface have been providing the ocean sciences communities with unprecedented insights into numerous processes and ocean applications (for more details see [1]). For instance, despite being a classical subject in physical oceanography, Internal Wave (IW) research has greatly benefited from

SAR evidence in the last few decades, especially when examining their generation, propagation, and dissipation mechanisms (see e.g., [2]). IWs may be regarded as density oscillations propagating along the ocean stratification, and it is now acknowledged that they impact a series of ocean phenomena ranging from fundamental oceanography to multiple other fields of research [3]. For instance, recent studies have revealed that they are increasingly important in quantifying and understanding ocean energetics and mixing [4,5]. Furthermore, recently quantified organic carbon fluxes that are associated with large IWs have been shown by Li et al. [6] to increase by as much as a factor of 3.

IW generation mechanisms in the ocean are of different kinds, and are still the subject of active discussion and research. An extensive review is beyond the scope of this paper, however it is important to note that IW observations in SAR are mostly tidal in origin—the reader is referred to the works by Jackson et al. [7] and da Silva et al. [2] for a comprehensive review of IW generation mechanisms. In this case, some of the IW generation details may be obtained via parameterized generation regimes, which are in turn based on characteristic measures of stratification, tidal currents, and bathymetry dimensions [8,9]. The topographic Froude number (Fr_t) and the normalized tidal excursion length (δ) are set as two major parameters governing the different IW generation regimes—defined as $\frac{N_{max}H}{U_{max}}$ and $\frac{U_{max}}{L\omega}$ (respectively), where N_{max} is a representative maximum of the buoyancy frequency, U_{max} is a typical value of the maximum flow velocity over some topography with characteristic width L and height H , and ω is usually the semi-diurnal tidal frequency. These non-dimensional parameters indicate that, for example, increasing or decreasing Fr_t means more or less blocking from the bathymetry on the incoming flow, or that the tidal excursion length is simply a measure of how much of the topography is traversed during a tidal excursion. A third parameter is also particularly important in the discussions to come. The internal or densimetric Froude number (Fr) is usually defined as U/c , and essentially describes the hydraulic state of a stratified flow with magnitude U (i.e., subcritical, critical, or supercritical) with respect to a characteristic IW phase speed (c). While these parameters are useful in describing IW generation in the vicinities of some bathymetry feature, they also define the upstream or downstream locations of the exact isopycnal perturbations from which IW trains eventually originate (also referred to as a lee wave or upstream influence). However, these details need not concern us here, especially since they are hard to determine from SAR imagery alone (i.e., without additional in situ or modelling data). What is particularly important for the observations discussed in this work is the resonant coupling between IWs of different vertical modes that has recently come to light from SAR imagery. This resonant coupling involves sea surface signatures of small-scale IWs that appear in between the larger IW packets usually observed in SAR, and it has been documented in the South China Sea [10] and in the Mascarene Ridge of the Indian Ocean [2]. In these independent studies, coupled IW systems propagating with similar phase speeds were documented by means of SAR and were investigated with numerical modelling. They are then said to be in resonant coupling in the sense that energy transfer between both IW systems is possible, with the larger-scale waves travelling deeper and the short-scale waves being trapped within the upper layers close to the ocean surface. In this paper, similar wave features will also be shown in the Andaman Sea.

The Andaman Sea in the Indian Ocean, located between the Malay Peninsula and the Andaman and Nicobar Islands (see Figure 1 for location), has been a classical study region for IWs for more than 50 years. However, observations of extraordinarily large IWs in this study region were reported long before their first scientific accounts. In fact, in 1861 the oceanographer Matthew F. Maury had already documented some large bands of choppy water or ripples stretching from horizon to horizon, which were commonly observed by mariners during their journeys in the Andaman Sea (see p. 389 in [11]). More than a century later, these descriptions were indeed recognized as the surface manifestation of large-scale and fast propagating IWs—when Perry and Schimke [12] conducted the first IW oceanographic measurements in this region. While aiming to determine the impact of IWs in underwater oil drilling structures, a series of measurements were also conducted by Osborne and Burch [13] in the southern edge of the Andaman Sea. Their detailed measurements revealed that these waves appeared in packets with ranking-ordered amplitudes, beginning at approximately 60 m in

the leading wave, and then decreasing towards the rear. These are characteristic features of Internal Solitary Waves (ISWs)—a special class of IWs which retain their shape and speed for considerable distances—which are usually described under the solitary wave theory of Korteweg and deVries (KdV). In fact, their measurements showed that these waves could be better predicted and interpreted under the shallow water KdV equation, and hence the term ISWs is usually referred to when describing the IWs propagating in the Andaman Sea.

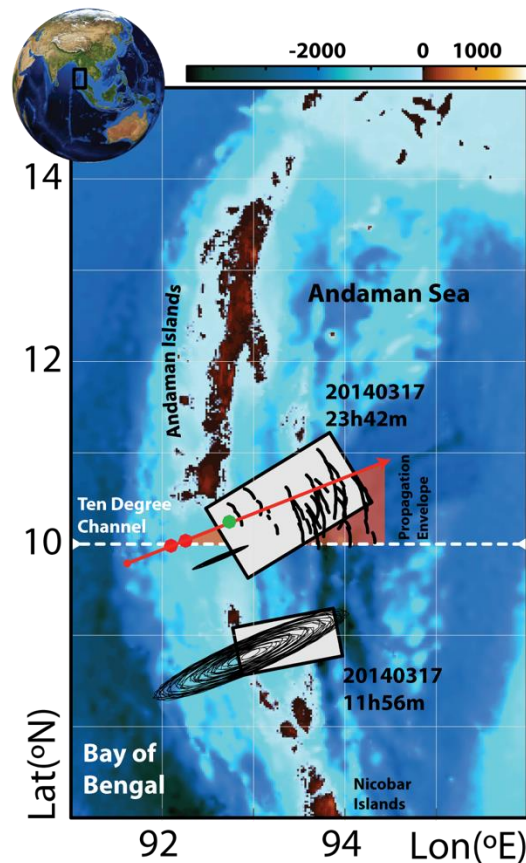


Figure 1. Bathymetry of the Andaman Sea corresponding to the inset on the top-left corner (colour-scaled on top). Grey rectangles depict subsets corresponding to TerraSAR-X acquisitions shown in Figure 3. Representative tidal ellipses are shown in black for a full spring-neap tidal cycle (the largest having a semi-major axis around 0.9 m/s). The red transect and colour-filled circles are reference locations discussed for a particular bathymetry profile shown in Figure 5.

Few other studies have emerged since. Particularly important are those by Alpers et al. [14] and Jackson [15], showing long SAR strips with exceptionally strong sea surface manifestations of ISW packets propagating onto the shelf of the Malayan Peninsula, suggesting tidally-driven generation sources in the western sections of the Andaman Sea. Acoustic Doppler Current Profiles presented by Neng et al. [16] also suggest IW sources near the shallow ridges separating the Andaman Sea from the Bay of Bengal, which were further confirmed in the high-resolution 3D numerical simulations shown in Shimizu and Nakayama [17]. Nonetheless, comprehensive descriptions of the IW fields are yet to be documented in this region—especially by means of SARs, which has been done in other equally important IW hotspots such as the South China Sea (e.g., [18]), the Mascarene Ridge in the Indian Ocean [2], and off the Amazon shelf [19].

Interestingly, however, global ocean models reveal IW energetics in this region to be at least of the same order as (if not greater than) those in other intensively studied regions (see e.g., [20]). In fact, in the particular case of the Andaman Sea (see Figure 1), a series of shallow ridges separate this marginal

sea from the Bay of Bengal along more than 1000 km—all of which are potential IW generation sites. Likewise, satellite views in this region typically reveal at least half a dozen distinct generation sites, almost resembling a series of ISW hotspots stacked meridionally—for example, shown in Jackson [15] and at <https://go.nasa.gov/2ow8eSK>. Furthermore, different characteristics can be found across these multiple generation sites involving important parameters such as bottom depth, bottom slopes, and tidal currents. This is especially interesting since direct comparisons can be made between different IW generation regimes while surveying them simultaneously in SAR imagery or other means of remote sensing.

Of particular interest to this study are two neighbouring and yet distinct stretches of the Andaman Sea—one approximately between 8° and 9°N, and the other along what is commonly referred to as the Ten Degree (10°) Channel (see Figure 1 for locations). In this study, we will show that these contiguous sections feature two very different ISW regimes. In fact, a recent survey using TerraSAR-X acquisitions—which are especially suited for ISW surveys as they deliver considerable wide swaths at very high spatial resolutions—from the Andaman Sea revealed a much more intricate structure than previously thought. In particular, evidence for resonant coupling between larger Internal Tides (ITs, i.e., IWs of tidal period) and shorter-scale mode-1 ISWs will be shown to be at work in the Andaman Sea, similar to recently documented cases in the South China Sea [10,21] and in the Mascarene Ridge [2]. Moreover, unprecedented SAR evidence will be shown that features short ISW envelopes with characteristic mode-2 sea surface signatures that are regularly spaced by higher-mode IWs.

In this paper, we seek to document the 2D horizontal structure on these particular sections of Andaman Sea (approximately between 8° and 11°N). The rest of the paper is organized as follows. Section 2 will describe the methods concerning satellite SAR imagery and important methodologies thereof. Section 3 will present key acquisitions that are representative of the study region, and a detailed analysis will follow in Section 4. Finally, Section 5 will summarise our main findings, along with some concluding remarks.

2. Methodology

Six SAR images that were acquired and processed from TerraSAR-X were selected as representative of the ISW activity in the Andaman Sea between 8° and 11°N. These are listed chronologically in Table 1, together with the Envisat-ASAR acquisition used in da Silva and Magalhaes [22], which is also especially important in this study (to be discussed in the next sections). All TerraSAR-X acquisitions were in ScanSAR-mode (with a nominal spatial resolution of 18 m), which means that the viewing strips were approximately 200 km wide and as long as 1000 km long in some cases. This acquisition mode is especially suited when surveying ISWs since wide swaths can be delivered with high spatial resolutions around tens of meters, allowing extended views of the waves along their propagation path, while preserving their detailed spatial structure.

ISWs are particularly well observed in SAR images, essentially owing to their characteristic sea surface manifestations (or signatures) in the short-scale (i.e., centimetre to decimetre) sea surface roughness, which is in turn proportional to the waves' surface current gradients [23–25]. An illustration is given in the schematic representation of Figure 2, which shows how the normalized radar cross section (σ_o) is modulated in the presence of mode-1 ISWs of depression (left panel in Figure 2)—as these are the most commonly observed in the ocean and in SAR images (see e.g., [15]). In this case, isopycnals are depressed as the wave propagates towards the right, while the wave's orbital velocity field creates a surface gradient with consecutive convergence and divergence sections. Consequently, sea surface roughness will increase and decrease in comparison with the unperturbed background. In a SAR image, when considering the wave direction of propagation (in agreement with [23]), this means mode-1 ISWs appear first as a bright and enhanced backscatter section, and after this a trailing dark and reduced backscatter section follows.

Table 1. List of images used in this study and in the composite map in Figure 1 (solid black lines). Tidal ranges within spring-neap cycles are given together with tidal currents (along the waves' direction of propagation) at time of acquisition. The number of wave-tail envelopes (N_{wt}) in each image is also shown with an averaged value for the length between consecutive wave-tails ($\bar{\lambda}$).

Acquisition Date/Time	Satellite Sensor & Mode	Tidal Range & Current	N_{wt} & $\bar{\lambda}$
2 January 2007 15h49m UTC	Envisat ASAR, Image Mode	+23 to −21 cm/s −5 cm/s	$N_{wt} = 4$ $\bar{\lambda} = 29$ km
17 March 2014 11h56m UTC (in Figure 3a)	TerraSAR-X TSX-SAR, ScanSAR	−22 to 23 cm/s +15 cm/s	$N_{wt} = 2$ $\bar{\lambda} = 30$ km
17 March 2014 23h42m UTC (in Figure 3b)	TerraSAR-X TSX-SAR, ScanSAR	−23 to +24 cm/s +14 cm/s	$N_{wt} = 5$ $\bar{\lambda} = 32$ km
1 April 2015 11h48m UTC	TerraSAR-X TSX-SAR, ScanSAR	−14 to +15 cm/s +15 cm/s	$N_{wt} = 3$ $\bar{\lambda} = 24$ km
23 April 2015 11h48m UTC	TerraSAR-X TSX-SAR, ScanSAR	−18 to +14 cm/s −9 cm/s	$N_{wt} = 2$ $\bar{\lambda} = 28$ km
4 May 2015 11h48m UTC	TerraSAR-X TSX-SAR, ScanSAR	−22 to +20 cm/s +15 cm/s	$N_{wt} = 1$ $\bar{\lambda} = NA$
4 May 2015 23h34m UTC	TerraSAR-X TSX-SAR, ScanSAR	−20 to 22 cm/s +17 cm/s	$N_{wt} = 3$ $\bar{\lambda} = 31$ km

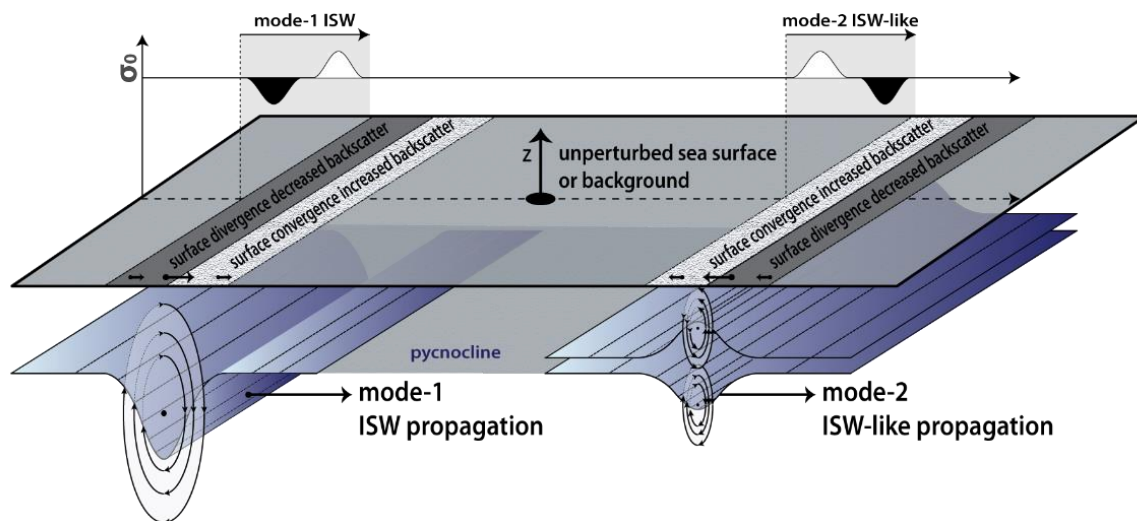


Figure 2. Schematic representation of Internal Solitary Wave (ISW) sea surface manifestations in Synthetic Aperture Radar (SAR) images with respect to an unperturbed background. A comparison between the mode-1 (left) and mode-2 (right) vertical structures is illustrated for waves propagating rightwards along the ocean pycnocline. From top to bottom, a measure for σ_0 is seen to depart from the background owing to the convergence and divergence patterns induced by the waves' surface currents—all of which reverse between mode-1 and mode-2 waves.

However, an increasing number of ISW observations have recently been documented in which SAR signatures are not consistent with this picture, and are instead reversed in relation to mode-1 ISWs. These waves are often discussed as resulting from a mode-2 internal vertical structure, and hence are termed mode-2 ISW-like waves, since they too usually appear in rank-ordered packets. According to Figure 2 (right panel), a convex mode-2 internal structure is best thought of as a bulge propagating along horizontally which displaces isopycnals upward and downward in the upper and lower layers, respectively. It is as if two individual ISWs are placed vertically on top of each other, and hence two orbital velocity fields appear instead. Only this time, the upper velocity field is reversed in relation

to the lower velocities, and hence in relation to typical mode-1 ISWs. In turn, this eventually means that the polarity of a mode-2 ISW-like wave signature at the surface is also reversed, meaning a dark reduced backscatter will precede bright enhanced backscatter in the propagation direction of the wave (see e.g., [2,26] for more details).

The information retrieved from SAR imagery can be analysed together with in situ data and linear theory to provide further insights into the generation and propagation details. In particular, if ISW packets are found regularly spaced in the images, then they are usually of tidal origin and their separations are interpreted as tidal wavelengths. In this case, travel-time plots (in the same fashion as in [2,27]) can be used to determine possible proxies for the waves' generation position and tidal phase. These can then be compared with the Baines [28] barotropic tidal forcing to determine the most likely ISW hotspots. The barotropic tidal forcing has been found to be a useful indicator for generation sites in other independent studies, including in the Iberian Shelf [29–32] and in the Mozambique Channel [33]. Following Baines [28], the barotropic forcing term (F) for ITs resulting from tidal currents and bottom bathymetry, is a scalar quantity found at each depth level as:

$$F(z) = zN^2(z) \int Q(x, y) \cdot \nabla \left(\frac{1}{h(x, y)} \right) dt \quad (1)$$

where z is the vertical coordinate (positive upwards), N is the buoyancy frequency, Q is the barotropic mass flux vector $Q = (uh, vh)$ with u and v being the zonal and meridional components of the barotropic velocity, and h the bottom depth. This tidal forcing is usually integrated analytically along a tidal cycle, provided that tidal currents are previously known and best-fitted to tidal ellipses. In this study, tidal currents were estimated from a regional solution for the Andaman Sea provided from the Oregon State University Tidal Inversion Software [34]), which runs at $1/30^\circ$ and includes 4 semidiurnal and 4 diurnal constituents ($M_2, S_2, N_2, K_2, K_1, O_1, P_1, Q_1$). The bathymetry data is part of the one minute global bathymetry from Smith and Sandwell [35], and the stratification was obtained from climatological monthly means (available at www.esrl.noaa.gov), which is assumed constant in the x (i.e., zonal) and y (i.e., meridional) directions in Equation (1).

According to this formulation, elevated barotropic forcing sites where ITs are being generated are usually found where large tidal currents oscillate across shallow steep bathymetry. This is certainly the case in the shallow ridges along the Andaman Sea (see Figure 1). Two distinct cases then follow, depending on how local stratification, bottom bathymetry, and tidal currents interact. Either the vertical oscillations induced in the water column radiate away horizontally in the form of interfacial waves directly along the nearby pycnocline, or IW beams (or rays) form and propagate coherently along an oblique direction to the horizontal [36]. In the first case, ocean ridges feature large interfacial ITs forming directly above steep bottom bathymetry, which typically evolve (through nonlinear processes) to higher-frequency ISW packets (see e.g., Figure 2 in [2]). Otherwise, when critical (or near-critical) slopes exist, meaning the bottom topographic slope matches the slope of the characteristic IT propagation paths, the IT energy propagates at an angle (θ) to the horizontal such that,

$$\tan \theta = \left(\frac{\omega^2 - f^2}{N^2 - \omega^2} \right)^{\frac{1}{2}} \quad (2)$$

where ω is the tidal frequency, f is the Coriolis parameter, and N is, again, the buoyancy frequency [36]. In other words, when the forcing barotropic flow is coincident with the motion plane for free IWs, resonant conditions usually result in enhanced IW beam generation. In continuously stratified fluids (such as the ocean), Equation (2) is often used in a ray tracing technique that follows IT beams, as these follow characteristic pathways along which the internal tide energy can propagate. These rays can then reflect from the seafloor or the sea surface, and interact afterwards with the ocean's pycnocline to generate ISWs by means of a different mechanism. Note that these ISWs do not originate from nearby bathymetry, but from IT beams instead, as these interact at an oblique angle with the ocean

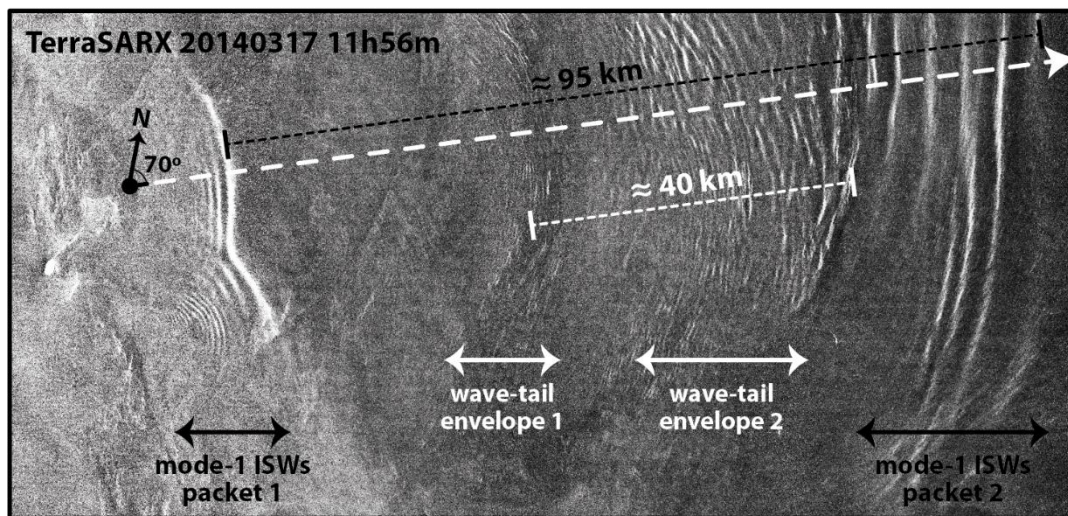
pycnocline, generating interfacial waves there that may evolve through nonlinear steepening into ISW packets. This mechanism is therefore usually referred to as *local generation* and it has been measured in situ [37,38], modelled numerically [39–41], and observed in laboratory experiments [42]. SAR imagery has confirmed its effectiveness as well, including in the Bay of Biscay, the Iberian shelf-break, and the Mozambique Channel [30,31,33,43].

More recently, in the Mascarene Ridge of the Indian Ocean, da Silva et al. [2] also found consistent evidence between SAR and fully nonlinear and non-hydrostatic simulations, showing large interfacial mode-2 IWs that originated from IT beams, interacting with the pycnocline from above after reflecting from the sea surface (see their Figure 9). It is noteworthy that these mode-2 features were found in resonant coupling with very short-scale mode-1 ISWs (meaning they both travelled at the same speed) which were clearly observed in SAR and referred to as wave-tails. This is especially important to the present study, since similar features will also be shown in this paper to be at work in the Andaman Sea. However, unlike the Mascarene Ridge, SAR observations of both mode-1 and mode-2 ISW-like waves will be shown to be recurring features in this study region—but they too will be consistent with resonance with higher-mode IWs.

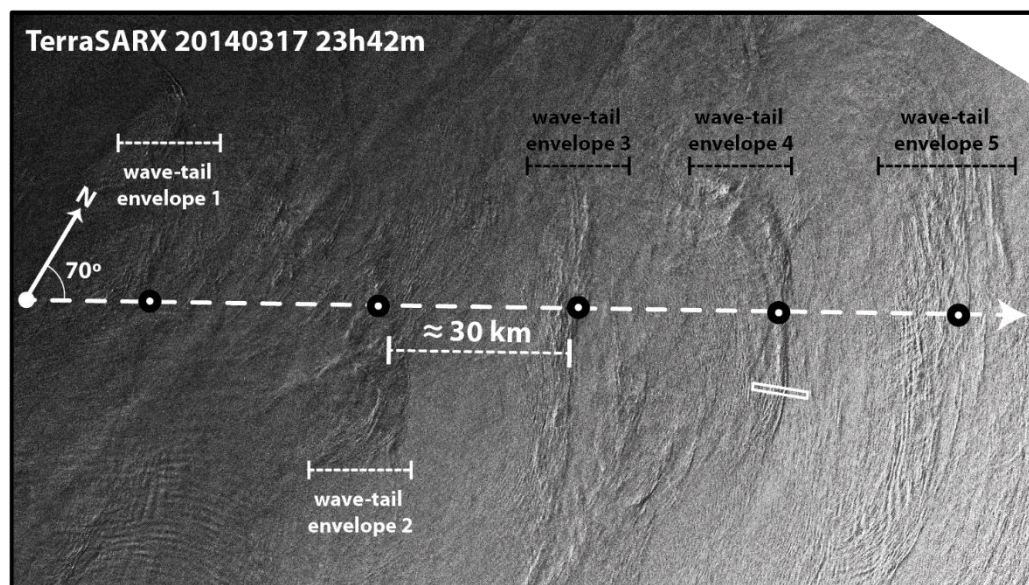
3. SAR Observations

We now present two selected case studies that are representative of the ISW field in the Andaman Sea between 8° and 11°N. These images show typical views along two adjacent stretches (see Figure 1 for locations), which will nonetheless appear very different. The first case study is presented in Figure 3a, and shows a TerraSAR-X image dated 17 March 2014, acquired as the satellite flew over the Andaman Sea (see also Supplemental Material S1). In this image, as in many others in this study region, two large mode-1 ISW packets may be seen, which are typically separated by 100 km along their propagation direction. A detailed inspection of the SAR signatures, in the same fashion as [44], reveals that the ISW packets propagate eastwards into the Andaman Sea and away from the shallow ridges near 9°N (see also the grey rectangle in Figure 1). Their backscatter modulations in the SAR consist essentially of very bright bands, behind which some less pronounced darker sections follow (especially in the easternmost wave). Considering that the ocean depths here are greater than 1000 m, this indicates that the sea surface signatures are consistent with mode-1 ISWs of depression. These large-scale packets are actually a typical view in the Andaman Sea, and are in fact very similar to those reported in other studies reporting similar IW activity in this region (e.g., [14,15]).

Careful examination reveals two other wave features in between the larger mode-1 ISW trains, which do not appear to belong to the same family of those. These are labelled as wave-tail envelopes in Figure 3a, owing to their wavy and clustered quasi-linear characteristics, whose total length along the propagation direction is at least 20 km. Their backscatter intensities are comparable to the larger ISWs, while still being characteristic of short-scale mode-1 ISWs of depression. Similar features have previously been reported in the South China Sea [10,21] and in the Mascarene Ridge [2]. In both cases, the authors also documented similar short-scale mode-1 ISWs, whose envelopes were seen to propagate coupled with larger mode-2 IWs (with a semidiurnal periodicity). Interestingly, the two wave-tails in Figure 3a were also separated by approximately half their larger mode-1 companions, and hence were consistent with a wavelength of a mode-2 IT. We also note in passing that these wave-tails are commonly observed in the Andaman Sea, including in other means of remote sensing as shown in Supplemental Material S2. In this case, an RGB composite (from MODIS) was acquired two days later in cloud free conditions, and again shows a wave-tail feature, this time a bit farther ahead its propagation path and in between two large mode-1 ISWs (almost identical to Figure 8 in [2]). As these features appear to be observed frequently in yet another region of the world's oceans, we feel that they add to the case that higher-mode IWs may be commonly operative in many other ISW hotspots.



(a)



(b)

Figure 3. (a) Subset of a TerraSAR-X image, approximately $123 \times 58 \text{ km}^2$, showing a typical view of the ISW field along 9°N in the Andaman Sea (see Figure 1 and Supplemental Material S1 for location). ISWs are propagating approximately towards 70°TN (white dashed arrow), and two mode-1 packets may be identified with a separating distance of roughly 100 km. In between these, two “wave-tail” envelopes are also depicted by white arrows and are spaced by about half of the previous wavelength; (b) Subset of a TerraSAR-X image, approximately $167 \times 94 \text{ km}^2$, showing a typical view of the ISW field along 10°N in the Andaman Sea (see Figure 1 for location). The wave field is propagating approximately towards 70°TN (white dashed arrow), but no mode-1 packets are observed. Instead, five regularly-spaced “wave-tail” envelopes are depicted by dashed borderlines. The white rectangle depicts the location of an ISW transect shown in Figure 4, and is consistent with a mode-2 ISW-like wave.

The second case study addressed in this paper presents an entirely different view. In this example, Figure 3b shows sea surface signatures that are typically observed along what is commonly referred to as the Ten Degree Channel of the Andaman Sea (see Figure 1 for location), corresponding to a TerraSAR-X image acquired approximately a semidiurnal tidal cycle later than Figure 3a. Nonetheless, unlike the previous case, the usual bright and large-scale mode-1 ISWs packets are all but missing.

Instead, the major features in this image are actually consistent with mode-2 short-period ISW-like waves. Indeed, while the IW field is also seen to propagate eastwards and away from the shallow ridges south of the Andaman Islands (c.f. Supplemental Material S3), the majority of the individual waves in this case have much shorter scales and their sea surface signatures are reversed when compared with those shown in Figure 3a. A detailed inspection of these sea surface signatures is presented in Figure 4. Recalling Figure 2, we note that the backscatter modulations along the waves in this case, reveal dark bands (i.e., decreased backscatter) preceding bright bands (i.e., increased backscatter) in the propagation direction, which for those deep-ocean conditions, are consistent with the sea surface manifestations of mode-2 ISW-like waves. Interestingly, despite the much shorter-scales and reduced packet coherency (comparing with larger mode-1 ISW packets), the profile in Figure 4 still suggests that these waves may have rank ordered amplitudes, at least in the leading and more prominent waves.

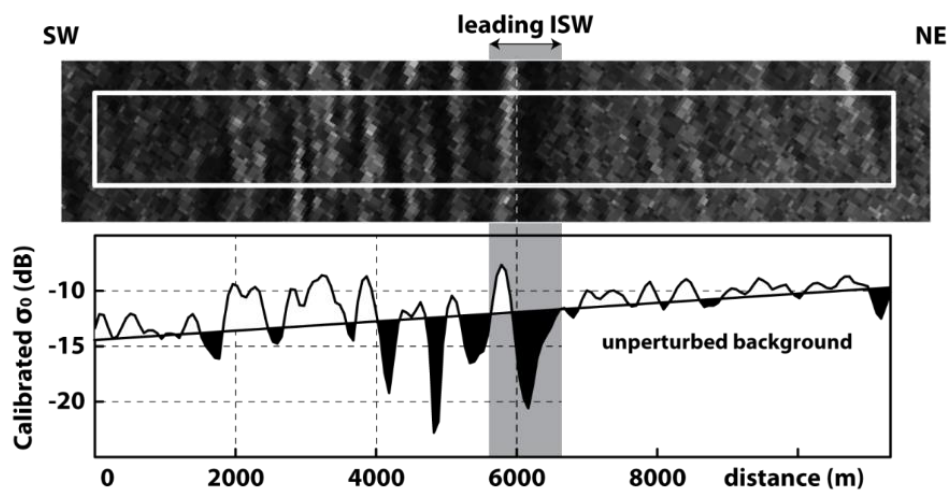


Figure 4. The top panel is a zoom in of the white rectangle in Figure 3b. The bottom panel is a transect along the white rectangle on top (extending approximately from the southwest to the northeast), showing a calibrated backscatter cross-section across a mode-2 ISW-like feature (leading wave highlighted in a grey background). The black line is a linear best fit used to illustrate signal modulation above (in white) and below (in black) a representative local average.

The IW field in Figure 3b is also very different from the traditional views of the Andaman Sea. Despite being acquired just north of Figure 3a (and a tidal cycle later), it is remarkable to see that no sign of large mode-1 ISW packets can be observed. Regularly-spaced envelopes still exist, but this time their average separations are roughly around 30 km, which are far from nominal mode-1 or even mode-2 IT wavelengths. Furthermore, five distinct envelopes may be identified, which means that the longevity of these wave-packets is at least 48 h (assuming semidiurnal periodicity). In fact, scrutiny suggests that the envelopes' characteristic dimensions increase from about 10 to more than 20 km as the waves develop along their direction of propagation. We stress that this represents an unprecedented view in the Andaman Sea and everywhere else in the ocean, in which five consecutive and regularly spaced mode-2 ISW-like wave envelopes were observed simultaneously in the same image.

Interestingly however, it is not an isolated event, but has instead been found in a number of images along this particular stretch of the Andaman Sea. Owing to their small-scale dimensions, these waves may have been overlooked in other remote sensing images. For instance, it is very hard to observe them in standard 250 m resolution sunglint images, where the larger mode-1 ISW packets are easily seen (see e.g., Supplemental Material S2). On the other hand, the enhanced radiometric resolution of the TerraSAR-X, alongside its wide coverage and detailed spatial resolutions, make it an ideal observational tool for these waves. In fact, after surveying the entire record, five more cases were identified with similar surface signatures consistent with mode-2 ISW-like waves—all of which

showed no signs of the larger mode-1 ISW packets. These are listed in Table 1 in chronological order, and span between 2014 and 2015. We note in passing that TerraSAR-X images were acquired only on 11 days throughout its entire record, which means that waves along the Ten Degree Channel were found on nearly 50% of these occasions. Furthermore, the tidal currents at the time of each acquisition are also listed in Table 1, and suggest that these mode-2 waves are found throughout the majority of the fortnightly tidal cycle. This is somewhat unexpected since the larger mode-1 ISW packets commonly observed in the Andaman Sea are known to be more frequently observed close to spring tides (see e.g., [13]). For consistency, one other image which is presented in da Silva and Magalhaes [22] is also presented in Table 1, and contains a very similar picture to that in Figure 3b.

A composite map consisting of all of the images listed in Table 1 is presented in Figure 1 (see solid black curves within the light red propagation envelope). In this map, only the leading and strongest observations were accounted for, and the mean distance between mode-2 ISW-like packet envelopes in each image ($\bar{\lambda}$) was also listed in Table 1, along with their corresponding number of observations (N_{WT}). It is worthwhile noting that these features consistently present interpacket distances of around 30 km, just as is observed in our case study in Figure 3b and in da Silva and Magalhaes [22]. Also, the composite map in Figure 1 reveals a well-organized IW field whose propagation envelope (in light red in Figure 1) is fairly along the tidal currents there, and suggests an origin along the shallow ridges to the west.

4. ISW Generation, Propagation, and Resonant Coupling

In general, the exact IW generation and propagation details cannot be confidently resolved without dedicated in situ measurements, modelling results, or a sufficiently large number of satellite images. Nonetheless, further evidence may be obtained from carefully inspecting the present dataset, especially in light of the methodologies described in the previous sections. The overall impression from the SAR is that substantial differences exist between the two IW fields depicted in Figure 3a,b (see Figure 1 for locations). While farther south, the SAR shows the usual mode-1 ISW packets propagating eastwards along with short-scale mode-1 wave-tails, the picture along the Ten Degree Channel is very different, since in this stretch only regularly spaced mode-2 ISW-like waves exist.

These short mode-2 ISW-like wave envelopes are an unprecedented view in this study region, and we therefore turn to the Ten Degree Channel since it is there that they are frequently observed. The observations in Figure 3b along this stretch reveal that the waves appear regularly spaced at about 30 km, which points to a tidal generation mechanism somewhere in the west shallow ridges south of the Nicobar Islands. A bathymetry profile along the waves propagation path (red transect in Figure 1) is shown in Figure 5a, and confirms a series of shallow ridges, all of which are potential IW generation sites. These can be further analysed by taking into consideration the methodologies discussed in the first sections. We begin by analysing the barotropic tidal forcing (F) along these shallow ridges, which is shown as an inset in Figure 5a. Recalling Section 2, we note that stratification in these calculations was assumed constant and was taken from a climatological mean for March (see Figure 5d)—taken as representative for the observed waves (see Table 1). The inset in Figure 5 then essentially shows the maxima depth integrated F along a full fortnightly cycle. The tidal forcing at the East Summit (ES) is especially strong, being above $1 \text{ m}^2 \text{ s}^{-2}$ for more than 10 km, and is in fact of the same order of other ISW hotspots in the Mozambique Channel (see Figure 4 in [33]). This indicates that energy is being converted from the barotropic tide into baroclinic motions at ES, which may then generate internal motions directly above the bathymetry, or evolve into IT beams (as discussed in the previous sections).

Both possibilities may be investigated by means of the parameters governing typical tidal generation regimes. Interestingly, in the case of ES and the mode-2 ISW-like waves observed in Figure 3b, both Fr and Fr_t are quite low, which is essentially a consequence of weak tidal currents (of the order of 10 cm/s, see Table 1) interacting with ES at depths where stratification itself is outside the bulk of the pycnocline. Namely, Fr is around 0.3 at most and Fr_t of the order of 100, when considering typical tidal currents and stratification, and characteristic phase speeds between 0.6 and 0.7 m/s—as

computed from the interpacket distances separating the mode-2 ISW-like waves in Figure 3b. Low internal and topographic Froude numbers suggest that it is unlikely that the waves seen in Figure 3b are being generated directly in the vicinities of ES (see [2,9]).

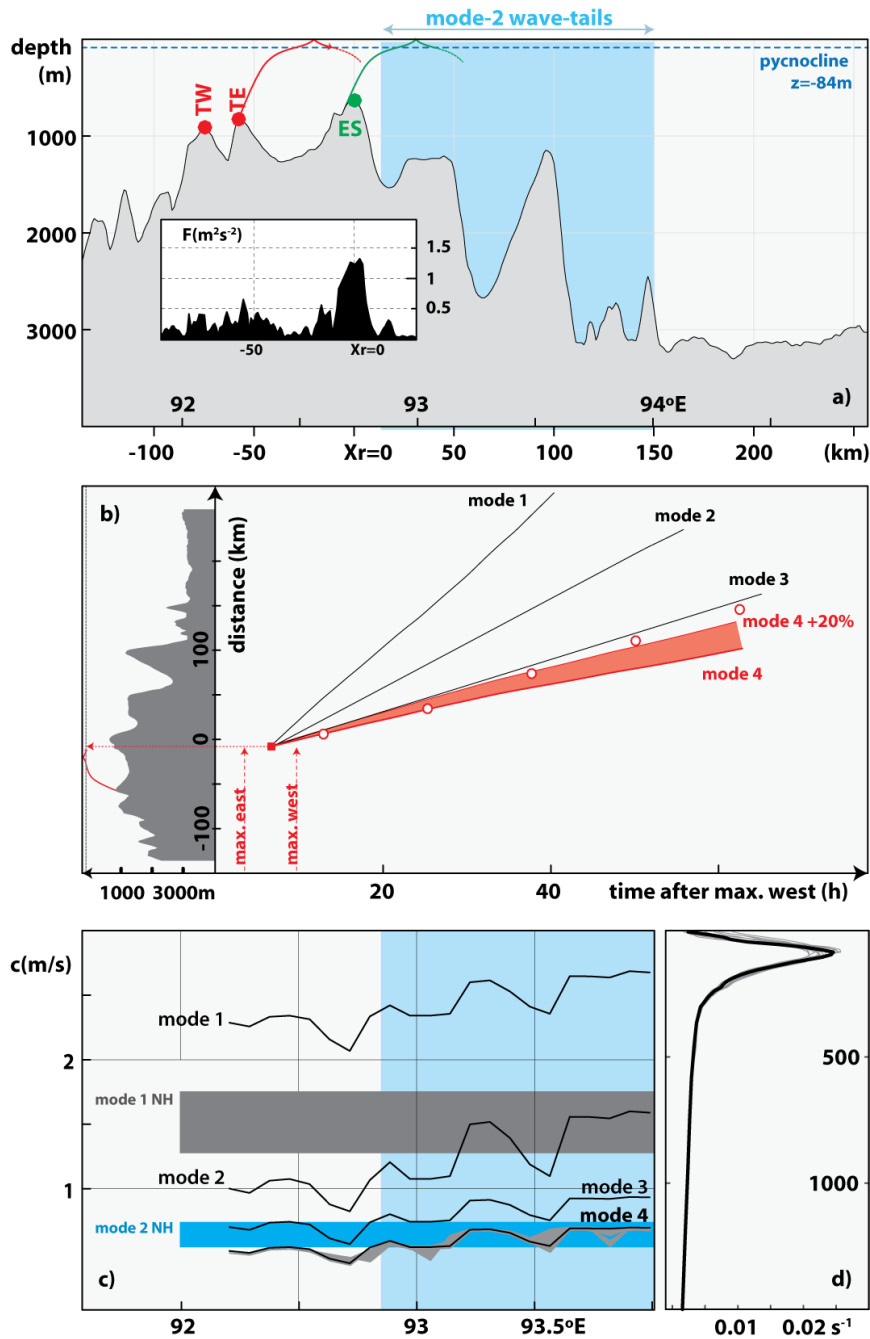


Figure 5. (a) Bathymetry profile along the red transect in Figure 1, including references to the East Summit (ES), Twin East (TE), and West (TW) summits. IT beams are also shown in corresponding colours, along with a representative pycnocline depth. The light blue shaded area depicts where the majority of the mode-2 observations are seen in the SAR; (b) Travel-time plot along the bathymetry profile in the top panel (see inset on left side); (c) Linear IW phase speeds for hydrostatic vertical modes 1–4 (solid black lines). Envelopes for the non-hydrostatic (NH) waves with wavelengths between 500 and 1500 m are also shown for modes 1 (grey) and 2 (blue); (d) March climatological mean stratification (solid black line), and remaining monthly means (in grey). See text for more details.

Alternatively, IT beams forming on critical slopes along these shallow features may be a suitable hypothesis instead, since tidal excursion lengths (δ) along these ridges appear to be of the order of 0.1. In the framework of IW generation regimes, this essentially translates to an optimum IT beam generation regime in the presence of critical (or near-critical) slopes (see e.g., [8] and Figure 6.36 in [45]). However, this means acknowledging the possibility that mode-2 ISW-like waves (rather than the usual mode-1 ISWs) could result from an IT beam impinging on the pycnocline and locally generating the waves there. Several studies have already documented the generation of waves with higher mode vertical structures in the vicinity of an IW beam impact, including in numerical models [41], laboratory experiments [42], and SAR imagery [2].

The above-mentioned studies indicate that mode-2 ISW-like waves may result from IT beams, provided that critical bathymetry exists from which IT beams can propagate and interact with the seasonal pycnocline in a geometric configuration consistent with the SAR observations—i.e., the waves observed in the SAR need to be ahead of the beam impact. Representative IT beams emanating from critical bathymetry in the vicinities of ES are depicted in green in Figure 5a as computed according to Equation (2), with the same mean stratification for March used in the barotropic tidal forcing calculations. However, interactions with the pycnocline in this case would be beyond (i.e., to the East of) the earliest SAR observations (see blue rectangle in Figure 5a), rendering this hypothesis less likely to be at work. A more promising possibility comes from ray tracing an IT beam from critical slopes farther west, in particular from TE (in red in Figure 5a) since interactions with the pycnocline there precede the SAR observations while still having a significant F around $0.5 \text{ m}^2 \text{ s}^{-2}$.

To verify consistency with the SAR ground truth, the summit location (TE in Figure 5a) can be investigated by means of a travel-time plot assembled in the same fashion as in [2,27], which allows for a proxy of the waves' propagation history to be reconstructed back to their point of origin. This is presented in Figure 5b for the five observations in Figure 3b (depicted as red circles). The data suggest a generation somewhat close to where the downward beam interacts with the pycnocline after it reflects from the surface at a time when the tide transitions from maximum east to westward flow (see also inset on the left-hand side of Figure 5b). This would mean that after maximum eastward flow, which is consistent with IT beams forming on the western slopes and leaning upwards to the east, mode-2 ISW-like waves result from the beam impact some 20 km before (i.e., to the west) the first observations are detected in the SAR—very similar to Figures 8 and 9 in [2].

However, it is important to note that the waves in Figure 5a are propagating over shallow and variable-depth bathymetry, which will alter their propagation speeds. Taking this into account means estimating phase speeds along variable bathymetry, which can be integrated numerically over time to yield an estimate for the waves' trajectories in a travel-time plot. In turn, this allows the waves in the SAR to be compared with the propagation predictions computed from linear theory as given by a standard boundary value problem, assuming the Taylor-Goldstein (TG) equation with appropriate boundary conditions as follows:

$$\frac{d^2\phi}{dz^2} + \left[\frac{N(z)^2}{(U-c)^2} - \frac{d^2U}{dz^2} - k^2 \right] \phi = 0, \quad \phi(0) = \phi(-H) = 0 \quad (3)$$

In this formulation, ϕ is the modal structure, k is the wavenumber representing the nonhydrostatic term, U is the current velocity along the waves' direction of propagation, c is a characteristic phase speed, and H is the bottom depth. In Figure 5b, distance versus time simulations are presented for the first four vertical modes assuming a semidiurnal tidal frequency and wavenumbers as observed from the SAR (set nominally to 30 km). The linear predicted trajectories presented as solid lines in Figure 5b reveal that the first three modes are too steep when compared with the observations, whereas their best fit is along a mode-4 long IW (solid line in red). Note that an increased wave speed is expected for the SAR observations when compared with those obtained from Equation (3), because of an additional contribution from nonlinearity. This effective wave speed increase due to nonlinearity is usually

around 20%, as documented in similar studies in other ISW hotspots (e.g., [2,27]), and it is indicated in Figure 5b as light red shades departing from the mode-4 solid red line. This corrected trajectory is quite consistent with the observations and propagation speeds around 0.7 m/s, just as estimated from the average spacing between the observations in Figure 3b. Interestingly, the solid red line representing a propagation trajectory consistent with a long mode-4 IW can be traced back in agreement with a generation close to where the downward beam interacts with the pycnocline, at a time when the tide transitions from maximum east to westward flow. We therefore believe this hypothesis is more consistent in light of the SAR, the in situ data, and the methodology described in Sections 1 and 2. We also note in passing that TW in Figure 5a yields very similar results (not shown). However, the Baines [28] body force (F) is slightly smaller around TW compared to TE, and we therefore do not pursue a generation hypothesis at TW here, leaving its detailed analysis for forthcoming investigations.

A closer inspection of Figure 5b indicates that the observations of mode-2 ISW-like waves extend for at least 100 km to the east, while enduring at least 48 h and 5 tidal cycles (assuming that the semidiurnal tide is at work). This is an unusually large time span when comparing with other mode-2 observations documented in the literature [2,46]. For instance, in da Silva et al. [2] some mode-2 ISW-like waves were found to be short-lived, not exceeding a single tidal-cycle, as were those documented off the coast of New Jersey with lifetimes typically less than a few hours [46]. The extended longevity observed in Figure 3b, and other images alike, could come from resonant conditions between the observed mode-2 wave-tails and larger mode-4 IWs (as indicated in Figure 5b). This hypothesis is inspired in recent studies such as Guo et al. [10] for the mode-1 wave-tails observed in the SAR, and larger mode-2 IWs that propagate along deeper water layers below in the South China Sea. In this particular stretch of the Andaman Sea, the effectiveness of this resonant coupling involving mode-2 short internal waves can be further investigated, even though the existence of a hypothetical mode-4 IW cannot be confirmed without dedicated in situ measurements or advanced numerical modelling.

Resonant conditions are usually discussed in the literature by comparing the phase speeds predicted according to Equation (3) for large IWs in hydrostatic mode (i.e., $k \approx 0$), with those predicted in a non-hydrostatic regime characteristic of the short-scale ISWs observed in the wave-tails (see [2,10,47]). In the case of Figure 3b, this means comparing large IWs with typical mode-4 wavelengths and mode-2 ISW-like wave-tails, which propagate along the direction of the red transect in Figure 1. Because the mode-2 ISW-like waves are long-lived, we choose to investigate resonant conditions along the waves' propagation path by comparing the characteristic phase speeds along the full extent of the IW field, as observed in the bottom profile in Figure 5a. This is done in Figure 5c for the same March stratification (see Figure 5d) by presenting phase speeds for the first four hydrostatic vertical modes (in solid black lines) along the bottom profile shown in Figure 5a, and the corresponding non-hydrostatic estimates assuming wavelengths between 500 and 1500 m, as observed in Figure 4 and in the SAR imagery listed in Table 1. Note that, while the hydrostatic case is somewhat sensitive to bathymetry changes, the shorter wavelengths in the non-hydrostatic cases are not—as expected based on linear IW theory. According to these results, the mode-2 ISW-like waves observed in the SAR have linear phase speed estimates (computed from Equation (3) and depicted in a light blue rectangle) close to both mode-3 and mode-4 long IWs (recalling their observed wavelengths is around 30 km in the SAR). However, they compare better with mode-4 when considering the full extent of the propagation path (especially to the East of 93°E). This means that the observations in the SAR are consistent with a resonant coupling predicted by linear theory between large mode-4 IWs and short-scale mode-2 ISW-like wave-tails. We also note that resonant conditions between mode-2 IWs and short mode-1 wave-tails (see grey shaded rectangle) exist, both along the Ten Degree Channel and farther south along the propagation path of the waves in Figure 3a. However, we reiterate that the SAR ground truth shows neither the usual large mode-1 ISW packets nor the mode-1 wave-tails along the Ten Degree Channel of the Andaman Sea.

According to the composite map in Figure 1, the waves' propagation envelope (depicted in light red) includes increasing eastward components than that corresponding to the profile in Figure 5a. For consistency then, ten more profiles corresponding to waves with more eastward components are analysed in Figure 5c, and correspond to the grey lines clustering around the hydrostatic mode-4 black curve which show that these too are fairly in resonant coupling with mode-2 ISW-like wave-tails. Furthermore, SAR shows these wave-tails to be observed, at least, from January to May in the Ten Degree Channel, and therefore similar plots were investigated for the remaining density profiles (climatological monthly means). In practice, this means having the pycnocline shifting some 50 m in the vertical and some 30% in the horizontal (see Figure 5d), while still yielding similar results to those in Figure 5c. This therefore adds to the robustness of the resonant coupling conditions in this region.

5. Summary and Conclusions

SAR imagery from TerraSAR-X is used to document the 2D horizontal structure of ISWs in the Andaman Sea between 8° and 11°N. According to the satellite imagery, two very distinct IW systems appear to be operating simultaneously in nearby stretches in this region. On the one hand, farther south the usual large mode-1 ISW packets are regularly observed, whereas mode-1 ISW wave-tails separated by long mode-2 wavelengths are also frequently observed, just as in other regions of the world's oceans. On the other hand, sea surface signatures in the SAR are very different along the Ten Degree Channel. In this case, no mode-1 ISW packets are apparent, while long-lived and regularly spaced mode-2 ISW-like wave-tails are frequently observed. These waves were analysed in light of additional in situ data and linear theory. While semidiurnal in nature, their generation appears to be more consistent with IT beams interacting with the local pycnocline, rather than resulting directly from the barotropic tide as it flows over the shallow ridges south of the Nicobar Islands. The unusually long-lived mode-2 wave-tails were also found consistent with a resonant coupling with larger mode-4 IWs. Altogether, we believe that this study region offers unique prospects as far as IW dynamics is concerned. In particular, several generation mechanisms could be operating simultaneously in close proximity, therefore providing SAR ground truth for forthcoming in situ measurements and/or numerical modelling. Evidence consistent with resonant coupling between different IW vertical structures in the Andaman Sea adds to an increasing awareness of the phenomenon in SAR observations, especially since in the Andaman Sea, they include simultaneous, multiple modes.

Supplementary Materials: The following are available online at <http://www.mdpi.com/2072-4292/10/6/861/s1>. S1: TerraSAR-X image shown in Figure 3a. S2: RGB composite from a MODIS-Terra image dated 2014/03/19. S3: TerraSAR-X image shown in Figure 3b.

Author Contributions: Both authors have equally contributed during all stages of this work.

Acknowledgments: The Authors would like to thank DLR projects OCE3154 and OCE2254 for providing the SAR images. This work was supported in part by FCT under Grant SFRH/BPD/84420/2012.

Conflicts of Interest: The authors declare no conflicts of interest.

References

1. Jackson, C.R.; Apel, J.R. *Synthetic Aperture Radar Marine User's Manual*; U.S. Department of Commerce: Washington, DC, USA, 2004; p. 464.
2. Da Silva, J.C.B.; Buijsman, M.C.; Magalhaes, J.M. Internal waves on the upstream side of a large sill of the Mascarene Ridge: A comprehensive view of their generation mechanisms and evolution. *Deep Sea Res.* **2015**, *99*, 87–104. [[CrossRef](#)]
3. Alford, M.H.; Peacock, T.; MacKinnon, J.A.; Nash, J.D.; Buijsman, M.C.; Centurioni, L.R.; Chao, S.Y.; Chang, M.H.; Farmer, D.M.; Fringer, O.B.; et al. The formation and fate of internal waves in the South China Sea. *Nature* **2015**, *521*, 65–69. [[CrossRef](#)] [[PubMed](#)]
4. Waterhouse, A.F.; MacKinnon, J.A.; Nash, J.D.; Alford, M.H.; Kunze, E.; Simmons, H.L.; Polzin, K.L.; St Laurent, L.C.; Sun, O.M.; Pinkel, R.; et al. Global patterns of mixing from measurements of the turbulent dissipation rate. *J. Phys. Oceanogr.* **2014**, *44*, 1854–1872. [[CrossRef](#)]

5. Kunze, E. Internal-Wave-Driven Mixing: Global Geography and Budgets. *J. Phys. Oceanogr.* **2017**, *47*, 1325–1345. [[CrossRef](#)]
6. Li, D.; Chou, W.-C.; Shih, Y.-Y.; Chen, G.-Y.; Chang, Y.; Chow, C.H.; Lin, T.-Y.; Hung, C.-C. Elevated particulate organic carbon export flux induced by internal waves in the oligotrophic northern South China Sea. *Nature* **2018**, *8*, 1–7. [[CrossRef](#)] [[PubMed](#)]
7. Jackson, C.R.; da Silva, J.C.B.; Jeans, G. The generation of nonlinear internal waves. *Oceanography* **2012**, *25*, 108–123. [[CrossRef](#)]
8. Nakamura, T.; Awaji, T.; Hatayama, T.; Akitomo, K.; Takizawa, T.; Kono, T.; Kawasaki, Y.; Fukasawa, M. The generation of large-amplitude unsteady lee waves by subinertial K1 tidal flow: A possible vertical mixing mechanism in the Kuril Straits. *J. Phys. Oceanogr.* **2000**, *30*, 1601–1621. [[CrossRef](#)]
9. Garrett, C.; Kunze, E. Internal tide generation in the deep ocean. *Annu. Rev. Fluid Mech.* **2007**, *39*, 57–87. [[CrossRef](#)]
10. Guo, C.; Vlasenko, V.; Alpers, W.; Stashchuk, N.; Chen, X. Evidence of short internal waves trailing strong internal solitary waves in the northern South China Sea from synthetic aperture radar observations. *Remote Sens. Environ.* **2012**, *124*, 542–550. [[CrossRef](#)]
11. Maury, M.F. *The Physical Geography of the Sea and Its Meteorology*; Harper: New York, NY, USA, 1861; p. 457.
12. Perry, R.B.; Schimke, G.R. Large-Amplitude Internal Waves Observed off the Northwest Coast of Sumatra. *J. Geophys. Res.* **1965**, *70*, 2319–2324. [[CrossRef](#)]
13. Osborne, A.R.; Burch, T.L. Internal Solitons in the Andaman Sea. *Science* **1980**, *208*, 451–460. [[CrossRef](#)] [[PubMed](#)]
14. Alpers, W.; Wang-Chen, H.; Hock, L. Observation of Internal Waves in the Andaman Sea by ERS SAR. IGARSS 97. *Remote Sens. Sci. Vis. Sustain. Dev.* **1997**, *4*, 1518–1520.
15. Jackson, C.R. *An Atlas of Internal Solitary-like Waves and Their Properties*, 2nd ed.; Global Ocean Associates: Alexandria, VA, USA, 2004; p. 560.
16. Yi-Neng, L.; Shi-Qiu, P.; Xue-Zhi, Z. Observations and Simulations of the Circulation and Mixing around the Andaman-Nicobar Submarine Ridge. *Atmos. Ocean. Sci. Lett.* **2012**, *5*, 319–323. [[CrossRef](#)]
17. Shimizu, K.; Nakayama, K. Effects of topography and Earth's rotation on the oblique interaction of internal solitary-like waves in the Andaman Sea. *J. Geophys. Res.* **2017**, *122*, 1–17. [[CrossRef](#)]
18. Jackson, C.R. An empirical model for estimating the geographic location of nonlinear internal solitary waves. *J. Atmos. Ocean. Technol.* **2009**, *26*, 2243–2255. [[CrossRef](#)]
19. Magalhaes, J.M.; da Silva, J.C.B.; Buijsman, M.C.; Garcia, C.A.E. Effect of the North Equatorial Counter Current on the generation and propagation of internal solitary waves off the Amazon shelf (SAR observations). *Ocean Sci.* **2016**, *12*, 243–255. [[CrossRef](#)]
20. Buijsman, M.C.; Ansong, J.K.; Arbic, B.K.; Richman, J.G.; Shriver, J.F.; Timko, P.G.; Wallcraft, A.J.; Whalen, C.B.; Zhao, Z.X. Impact of parameterized internal wave drag on the semidiurnal energy balance in a global ocean circulation model. *J. Phys. Oceanogr.* **2016**, *46*, 1399–1419. [[CrossRef](#)]
21. Vlasenko, V.; Stashchuk, N.; Guo, C.; Chen, X. Multimodal structure of baroclinic tides in the South China Sea. *Nonlinear Process. Geophys.* **2010**, *17*, 529–543. [[CrossRef](#)]
22. Da Silva, J.C.B.; Magalhaes, J.M. Internal solitons in the Andaman Sea: A new look at an old problem. *Proc. SPIE* **2016**. [[CrossRef](#)]
23. Alpers, W. Theory of radar imaging of internal waves. *Nature* **1985**, *314*, 245–247. [[CrossRef](#)]
24. Da Silva, J.C.B.; Ermakov, S.A.; Robinson, I.S.; Jeans, D.R.G.; Kijashko, S.V. Role of surface films in ERS SAR signatures of internal waves on the shelf: 1. Short-period internal waves. *J. Geophys. Res.* **1998**, *103*, 8009–8031. [[CrossRef](#)]
25. Da Silva, J.C.B.; Ermakov, S.A.; Robinson, I.S. Role of surface films in ERS SAR signatures of internal waves on the shelf: 3. Mode transitions. *J. Geophys. Res.* **2000**, *105*, 24089–24104. [[CrossRef](#)]
26. Jackson, C.R.; da Silva, J.C.B.; Jeans, G.; Alpers, W.; Caruso, M.J. Nonlinear Internal Waves in Synthetic Aperture Radar Imagery. *Oceanography* **2013**, *26*, 68–79. [[CrossRef](#)]
27. Da Silva, J.C.B.; New, A.L.; Magalhaes, J.M. On the structure and propagation of internal solitary waves generated at the Mascarene Plateau in the Indian Ocean. *Deep Sea Res.* **2011**, *58*, 229–240. [[CrossRef](#)]
28. Baines, P.G. On internal tide generation models. *Deep Sea Res.* **1982**, *29*, 307–338. [[CrossRef](#)]
29. Sherwin, T.J.; Vlasenko, V.I.; Stashchuk, N.; Jeans, D.R.G.; Jones, B. Along-slope generation as an explanation for some unusually large internal tides. *Deep Sea Res.* **2002**, *49*, 1787–1799. [[CrossRef](#)]

30. Azevedo, A.; da Silva, J.C.B.; New, A.L. On the generation and propagation of internal solitary waves in the southern Bay of Biscay. *Deep Sea Res.* **2006**, *53*, 927–941. [[CrossRef](#)]
31. Da Silva, J.C.B.; New, A.L.; Azevedo, A. On the role of SAR for observing local generation of internal solitary waves off the Iberian Peninsula. *Can. J. Remote Sens.* **2007**, *33*, 388–403. [[CrossRef](#)]
32. Magalhaes, J.M.; da Silva, J.C.B. SAR observations of internal solitary waves generated at the Estremadura Promontory off the west Iberian coast. *Deep Sea Res.* **2012**, *69*, 12–24. [[CrossRef](#)]
33. Da Silva, J.C.B.; New, A.L.; Magalhaes, J.M. Internal solitary waves in the Mozambique Channel: Observations and interpretation. *J. Geophys. Res.* **2009**, *114*, C05001. [[CrossRef](#)]
34. Egbert, G.D.; Erofeeva, S.Y. Efficient inverse modeling of barotropic ocean tides. *J. Ocean. Atmos. Technol.* **2002**, *19*, 183–204. [[CrossRef](#)]
35. Smith, W.H.F.; Sandwell, D.T. Global sea floor topography from satellite altimetry and ship depth soundings. *Science* **1997**, *277*, 1956–1962. [[CrossRef](#)]
36. Leblond, P.H.; Mysak, L.A. *Waves in the Ocean*; Elsevier: New York, NY, USA, 1978; Volume 20, p. 602.
37. New, A.L.; Pingree, R.D. Large-amplitude internal soliton packets in the central Bay of Biscay. *Deep Sea Res.* **1990**, *37*, 513–524. [[CrossRef](#)]
38. New, A.L.; Pingree, R.D. Local generation of internal soliton packets in the central Bay of Biscay. *Deep Sea Res.* **1992**, *39*, 1521–1534. [[CrossRef](#)]
39. Gerkema, T. Internal and interfacial tides: Beam scattering and local generation of solitary waves. *J. Mar. Res.* **2001**, *59*, 227–255. [[CrossRef](#)]
40. Akylas, T.R.; Grimshaw, R.H.J.; Clark, S.R.; Tabaei, A. Reflecting tidal wave beams and local generation of solitary waves in the ocean thermocline. *J. Fluid Mech.* **2007**, *593*, 297–313. [[CrossRef](#)]
41. Grisouard, N.; Staquet, C.; Gerkema, T. Generation of internal solitary waves in a pycnocline by an internal wave beam: A numerical study. *J. Fluid Mech.* **2011**, *676*, 491–513. [[CrossRef](#)]
42. Mercier, M.J.; Mathur, M.; Gostiaux, L.; Gerkema, T.; Magalhaes, J.M.; da Silva, J.C.B.; Dauxois, T. Soliton generation by internal tidal beams impinging on a pycnocline: Laboratory experiments. *J. Fluid Mech.* **2012**, *704*, 37–60. [[CrossRef](#)]
43. New, A.L.; da Silva, J.C.B. Remote-sensing evidence for the local generation of internal soliton packets in the central Bay of Biscay. *Deep Sea Res.* **2002**, *49*, 915–934. [[CrossRef](#)]
44. Thompson, D.R.; Gasparovic, R.F. Intensity modulation in SAR images of internal waves. *Nature* **1986**, *320*, 345–348. [[CrossRef](#)]
45. Vlasenko, V.; Stashchuk, N.; Hutter, K. *Baroclinic Tides: Theoretical Modeling and Observational Evidence*; Cambridge University Press: New York, NY, USA, 2005; p. 351.
46. Shroyer, E.L.; Moum, J.N.; Nash, J.D. Mode 2 waves on the continental shelf: Ephemeral components of the nonlinear internal wave field. *J. Geophys. Res.* **2010**, *115*, C07001. [[CrossRef](#)]
47. Pingree, R.D.; Mardell, J.T.; New, A.L. Propagation of internal tides from the upper slopes of the Bay of Biscay. *Nature* **1986**, *321*, 154–158. [[CrossRef](#)]



© 2018 by the authors. Licensee MDPI, Basel, Switzerland. This article is an open access article distributed under the terms and conditions of the Creative Commons Attribution (CC BY) license (<http://creativecommons.org/licenses/by/4.0/>).